DOI: 10.5028/jatm.2009.0102135152

João Luiz F. Azevedo*
Institute of Aeronautics and Space
São José dos Campos – Brazil
azevedo@iae.cta.br

Heidi Korzenowski
VSE- Vale Solutions in Energy
São José dos Campos – Brazil
heidi.korzenowski@vsesa.com.br

*author for correpondence

An assessment of unstructured grid finite volume schemes for cold gas hypersonic flow calculations

Abstract: *A comparison of five different spatial discretization schemes is performed considering a typical high speed flow application. Flowfields are simulated using the 2-D Euler equations, discretized in a cell-centered finite volume procedure on unstructured triangular meshes. The algorithms studied include a central difference-type scheme, and 1st- and 2nd-order van Leer and Liou flux-vector splitting schemes. These methods are implemented in an efficient, edge-based, unstructured grid procedure which allows for adaptive mesh refinement based on flow property gradients. Details of the unstructured grid implementation of the methods are presented together with a discussion of the data structure and of the adaptive refinement strategy. The application of interest is the cold gas flow through a typical hypersonic inlet. Results for different entrance Mach numbers and mesh topologies are discussed in order to assess the comparative performance of the various spatial discretization schemes.*

Keywords: *Hypersonic flow, Cold gas flow, Finite volume method, Unstructured grids, Spatial discretization schemes.*

INTRODUCTION

The present work considers that the flowfields of interest are simulated using the 2-D Euler equations. For such hyperbolic equations, the physical propagation of perturbations occurs along characteristic lines. The schemes based on central spatial discretizations possess symmetry with respect to a change in sign of the Jacobian matrix eigenvalues which does not distinguish upstream from downstream influences. In such case, these schemes do not consider physical properties of the flow equations into the discretized formulation and this generates oscillations in the vicinity of discontinuities which have to be damped by the addition of artificial dissipation terms. The problem is, therefore, to determine the adequate amount of artificial dissipation which should be large enough to damp instabilities and, at the same time, small enough to avoid the destruction of flow features.

Upwind schemes take into account physical properties in the discretization process and they have the advantage of being naturally dissipative. Flux vector splitting methods introduce the information of the sign of the eigenvalues in the discretization process, and the flux terms are split and discretized according to the sign of the associated propagation speeds. Steger and Warming (see, for instance, Steger and Warming, 1981, and Hirsch, 1990) make use of the homogeneous property of the Euler equations and split the flux vectors into forward and backward contributions by splitting the eigenvalues of the Jacobian matrix into non-negative and non-positive groups. The split flux contributions are, then, spatially differentiated according to one-sided upwind discretizations. However, these forward and backward fluxes are not differentiable when an eigenvalue changes sign, and this can produce oscillations at sonic points. In order to avoid these oscillations, van Leer (1982) determines a continuously spatially differenced flux vector splitting that leads to smoother solutions at sonic points.

In the present work, the interface fluxes are calculated using five different algorithms, including a central difference-type scheme, and van Leer (1982) and Liou (1996) flux vector splitting schemes. In the central difference case, the interface fluxes are obtained from an average vector of conserved variables at the interface, which is calculated by straightforward arithmetic averages of the vector of conserved variables on both sides of the interface. Since this approach provides no numerical dissipation terms to control nonlinear instabilities, an appropriate blend of undivided Laplacian and biharmonic operators is explicitly added as the necessary artificial dissipation terms. For the first-order van Leer scheme, the interface fluxes are obtained by van Leer's formulas (van Leer, 1982) and they are constructed using the conserved properties for the *i*-th control volume and its neighbor across the given

Received: 03/09/09
Accepted: 06/10/09

interface. The second order scheme considers a MUSCL approach (Anderson, Thomas and van Leer, 1986), that is, the interface fluxes are formed using left and right states at the interface, which are linearly reconstructed by primitive variable extrapolation on each side of the interface. The extrapolation process is effected by a limiter in order to avoid the creation of new local extrema. The first- and second-order Liou schemes consider that the convective operator can be written as a sum of the convective and pressure terms (Liou, 1996). The second-order scheme also considers a MUSCL approach.

The Euler equations are discretized in a cell-centered finite-volume-based procedure on unstructured triangular meshes. Time march uses a fully explicit, 2nd-order accurate, five-stage Runge-Kutta time stepping scheme. Only steady-state calculations have been considered in the present context, and variable time stepping and implicit residual smoothing procedures have been employed to accelerate convergence to steady-state. Computations using a fine, fixed, unstructured mesh are compared to those obtained with an adaptive mesh procedure in order to assess the quality of the solutions calculated by the different schemes implemented and in order to analyze the mesh influence in the capture of the flow features of interest.

The schemes discussed here are applied to the solution of supersonic/hypersonic inlet flows. A 2-D inlet configuration which is representative of some proposed inlet geometries for a typical transatmospheric vehicle is considered. The inlet entrance conditions were varied from a freestream Mach number $M_\infty = 4$ up to $M_\infty = 16$ in order to test the schemes implemented for a wide range of possible inlet operating conditions. The fluid was treated as a perfect gas and, hence, no chemistry was taken into account. From a physical standpoint, the present simulations are typical of cold gas flows which are usually achieved in experimental facilities such as gun tunnels. This is certainly not representative of actual flight conditions in which dissociation and vibrational relaxation are important phenomena, especially for the higher Mach number cases. However, it is a necessary step in order to construct a robust code to deal with the complete environment encountered in actual flight.

THEORETICAL FORMULATION

The 2-D time dependent Euler equations can be written in integral form as

$$\frac{\partial}{\partial t}\int_V Q\,dV + \int_V \left(\vec{\nabla}\cdot\vec{P}\right) dV = 0, \tag{1}$$

where $\vec{P} = E\hat{\imath} + F\hat{\jmath}$. The application of the divergence theorem to Eq. (1) will yield

$$\frac{\partial}{\partial t}\int_V Q\,dV + \int_S \left(\vec{P}\cdot\vec{n}\right) dS = 0, \tag{2}$$

where V represents the area of the control volume, S is its boundary and $\vec{n}$ is the outward normal to the S boundary.

The vector of conserved quantities, Q, and the convective flux vectors, E and F, are given by

$$Q = \left[\begin{array}{cccc} \rho & \rho u & \rho v & e \end{array}\right]^T, \tag{3}$$

$$E = \left\{\begin{array}{c} \rho u \\ \rho u^2 + p \\ \rho uv \\ (e+p)\,u \end{array}\right\}, \quad F = \left\{\begin{array}{c} \rho v \\ \rho uv \\ \rho v^2 + p \\ (e+p)\,v \end{array}\right\}. \tag{4}$$

Here, ρ denotes the density, p is the pressure, u and v represent the Cartesian velocity components, and e is the total energy per unit of volume.

If the equations are discretized using a cell-centered finite-volume-based procedure, the discrete vector of conserved variables, Q_i, is defined as an average over the i-th control volume as

$$Q_i = \frac{1}{V_i}\int_{V_i} Q\,dV. \tag{5}$$

In this context, the discrete flow variables can be assumed as attributed to the centroid of each cell if necessary. With the previous definition of Q_i, Eq. (2) can be rewritten for the i-th volume as

$$\frac{\partial}{\partial t}\left(V_i Q_i\right) + \int_{S_i}\left(E\,dy - F\,dx\right) = 0. \tag{6}$$

SPATIAL DISCRETIZATION ALGORITHMS

Spatial discretization is essentially concerned with finding a discrete approximation to the surface integral in Eq. (6). This approximation is the so-called convective operator, $C(Q_i)$, i.e.,

$$C(Q_i) \cong \int_{S_i}\left(E\,dy - F\,dx\right). \tag{7}$$

Centered Scheme

In the centered scheme case, the convective operator is defined as

$$C(Q_i) = \sum_{k=1}^{3}\left[E(Q_{ik})\,\Delta y_{ik} - F(Q_{ik})\,\Delta x_{ik}\right]. \tag{8}$$

In this expression, Q_{ik} is the arithmetic average of the conserved properties in the cells which share the ik

interface, where i is the i-th control volume and k is its neighbor. The terms Δx_{ik} and Δy_{ik} are calculated as

$$\Delta x_{ik} = (y_{k2} - y_{k1}), \qquad \Delta y_{ik} = (x_{k2} - x_{k1}), \quad (9)$$

where the points (x_{k1}, y_{k1}) and (x_{k2}, y_{k2}) are the vertices which define the interface between cells i and k (Azevedo, 1992).

The spatial discretization procedure presented in Eq. (8) is equivalent to a central difference scheme. Therefore, artificial dissipation terms must be added in order to control nonlinear instabilities (Jameson and Mavriplis, 1986). In the present case, the artificial dissipation operator, $D(Q_i)$, is formed as a blend of undivided Laplacian and biharmonic operators (Mavriplis, 1988, and Mavriplis, 1990). These mimic, in an unstructured mesh context, the concept of using second and fourth difference terms (Jameson, Schmidt and Turkel, 1981, and Pulliam, 1986). Therefore, the artificial dissipation operator is given by

$$D(Q_i) = d^{(2)}(Q_i) - d^{(4)}(Q_i), \quad (10)$$

where $d^{(2)}(Q_i)$ represents the contribution of the Laplacian operator and $d^{(4)}(Q_i)$ represents the contribution of biharmonic operator.

In order to form the biharmonic operator, it is necessary to first define the undivided Laplacian operator for the i-th control volume as

$$\nabla^2 Q_i = \sum_{k=1}^{3} (Q_k - Q_i), \quad (11)$$

where the summation in k is taken over all control volumes which have a common interface with the i-th cell. The biharmonic operator is, then, defined as (Azevedo, 1992, and Azevedo and Oliveira, 1994)

$$d^{(4)}(Q_i) = \sum_{k=1}^{3} \frac{\epsilon_{ik}^{(4)}}{2} \left(\frac{V_i}{\Delta t_i} + \frac{V_k}{\Delta t_k} \right) (\nabla^2 Q_k - \nabla^2 Q_i) \quad (12)$$

The Laplacian operator is responsible for avoiding oscillations near discontinuities and it is constructed as

$$d^{(2)}(Q_i) = \sum_{k=1}^{3} \frac{\epsilon_{ik}^{(2)}}{2} \left(\frac{V_i}{\Delta t_i} + \frac{V_k}{\Delta t_k} \right) (Q_k - Q_i). \quad (13)$$

Here, the coefficient $\epsilon_{ik}^{(2)}$ is given by

$$\epsilon_{ik}^{(2)} = K^{(2)} \max(\nu_i, \nu_k), \quad (14)$$

where the switching function ν_i is defined in terms of the local pressure gradient as

$$\nu_i = \frac{\sum_{k=1}^{3} |p_k - p_i|}{\sum_{k=1}^{3} (p_k + p_i)}. \quad (15)$$

Close to discontinuities, the biharmonic operator produces oscillations. Therefore, the coefficient $\epsilon_{ik}^{(4)}$ is defined such that it is switched off when the second difference coefficient, $\epsilon_{ik}^{(2)}$, becomes large. This typically occurs near shocks or other discontinuities. The $\epsilon_{ik}^{(4)}$ coefficient is defined as

$$\epsilon_{ik}^{(4)} = \max\left[0, \left(K^{(4)} - \epsilon_{ik}^{(2)}\right)\right]. \quad (16)$$

Typical values for the constants (Mavriplis, 1988) are $K^{(2)} = 1/4$ and $K^{(4)} = 3/256$.

First-Order Van Leer Scheme

The convective operator, $C(Q_i)$, is defined for the van Leer flux vector splitting scheme (van Leer, 1982, and Anderson, Thomas and van Leer, 1986) by the expression

$$C(Q_i) = \sum_{k=1}^{3} (E_{ik}\, \Delta y_{ik} - F_{ik}\, \Delta x_{ik}), \quad (17)$$

where Δx_{ik} and Δy_{ik} are given by Eq. (9). In the present case, the interface fluxes, E_{ik} and F_{ik}, are defined as (Azevedo and Figueira da Silva, 1997)

$$\begin{aligned} E_{ik} &= \begin{cases} E_i^+ + E_k^- & \text{for } \Delta y_{ik} \geq 0 \\ E_k^+ + E_i^- & \text{for } \Delta y_{ik} < 0 \end{cases}, \\ F_{ik} &= \begin{cases} F_i^+ + F_k^- & \text{for } \Delta x_{ik} \leq 0 \\ F_k^+ + F_i^- & \text{for } \Delta x_{ik} > 0 \end{cases}. \end{aligned} \quad (18)$$

Here, $E_i^{\pm}$ and $F_i^{\pm}$ are the split fluxes calculated using van Leer's formulas (van Leer, 1982, and Anderson, Thomas and van Leer, 1986) and the conserved properties of the i-th control volume. The evaluation of the split fluxes in the van Leer context can be summarized as follows:

$$\begin{aligned} M_x \geq 1 \quad &\Rightarrow \quad E^+ = E \quad \text{and} \quad E^- = 0, \\ M_x \leq -1 \quad &\Rightarrow \quad E^+ = 0 \quad \text{and} \quad E^- = E, \\ |M_x| < 1 \quad &\Rightarrow \quad E^{\pm} = \begin{Bmatrix} f^{\pm} \\ \left(f^{\pm}\left[(\gamma-1)\,u \pm 2a\right]\right)/\gamma \\ f^{\pm} v \\ f^{\pm}\left[\frac{\{(\gamma-1)u \pm 2a\}^2}{\{2(\gamma^2-1)\}} + \frac{v^2}{2}\right] \end{Bmatrix}. \end{aligned} \quad (19)$$

In the previous equations, the Mach number in the x-direction is defined as $M_x = u/a$ and the split mass fluxes are $f^{\pm} = \pm \rho a\, [(M_x^{\pm} 1)/2]^2$. Similar expressions are obtained for $F^{\pm}$ using $M_y = v/a$. With this flux vector definition, the splitting is continuously differentiable at sonic and stagnation points.

Second-Order Van Leer Scheme

In the present work, the implementation of the 2nd-order van Leer scheme is based on an extension of the Godunov approach. The projection stage of the Godunov scheme, in which the solution is projected in each cell on piecewise constant states, is modified. This constitutes the so-called MUSCL (Monotone Upstream-Centered Scheme for Conservation Laws) approach (van Leer, 1979) for the extrapolation of primitive variables. By this approach, left and right states at a given interface are linearly reconstructed by primitive variable extrapolation on each side of the interface, together with some appropriate limiting process (Hirsch, 1990) in order to avoid the generation of new extrema. The vector of primitive variables is taken as $W = [p, u, v, T]^T$, in the present case. The convective operator, $C(Q_i)$, can be defined as indicated in Eq. (17). The interface fluxes, E_{ik} and F_{ik}, are defined as

$$\begin{aligned} E_{ik} &= E^+(Q_L) + E^-(Q_R), \\ F_{ik} &= F^+(Q_L) + F^-(Q_R), \end{aligned} \qquad (20)$$

where $Q_L = Q(W_L)$ and $Q_R = Q(W_R)$ are the left and right states at the *ik* interface obtained by the linear extrapolation process previously discussed.

There are two aspects of the unstructured grid implementation of such a scheme which deserve further consideration. The first aspect concerns the definition of "left" and "right" states at a given cell interface. Since there is no concept similar to curvilinear coordinates in this case, the cell interfaces can have virtually any orientation and one must decide which way to "look" in order to construct left and right states. This is done in the present case based on the components of the vector normal to the edge, as already indicated in Eq. (18) for the 1st-order van Leer scheme. The other aspect is associated with deciding which second control volume will be used for the reconstruction process in addition to the volume immediately adjacent to the interface considered. The authors emphasize that an edge-based data structure (Mavriplis, 1988) is being used in this development and further discussion of the data structure used will be presented later in the paper.

The procedure adopted in the present case to handle the second aspect is inspired by the work of Lyra (1994). The major difference between the present implementation and the cited reference lies in the direction in which the one-dimensional stencil is constructed. In Lyra (1994), the stencil for extrapolation is constructed along the direction of the edge. It must be emphasized that Lyra (1994) is working with a finite element approach. Here, since a cell-centered finite volume method is of interest, the extrapolation stencil is constructed in a direction normal to the edge. In an attempt to reinterpret the 1-D ideas in the present unstructured grid context, a line is drawn normal to the edge and passing through the center of the inscribed circle. A third point is located over this line at a distance from the center of the inscribed circle equal to the diameter of the circle. The code, then, identifies in which control volume this 3rd point lies, and it uses the properties of this triangle in the linear reconstruction of the primitive variables.

In order to make the nomenclature clear, the two triangles which are adjacent to the edge under consideration are denoted *i* and *k*. The second triangle identified by the previously described process and associated with triangle *i* is denoted *l*. The corresponding one associated with k is denoted triangle *m*. This is illustrated in Fig. 1. Therefore, in the calculation of the $E^{\pm}$ fluxes, the left state, Q_L, is defined using the properties of the *i* and *l* triangles and the right state, Q_R, is defined using those of the *k* and *m* triangles, if $\Delta y_{ik} \geq 0$. The reverse is true if $\Delta y_{ik} < 0$. Similarly, the definition of the $F^{\pm}$ fluxes uses data at the *i* and *l* triangles to define the left state and data at the *k* and *m* triangles to define the right state if $\Delta x_{ik} \leq 0$, and vice-versa if $\Delta x_{ik} > 0$.

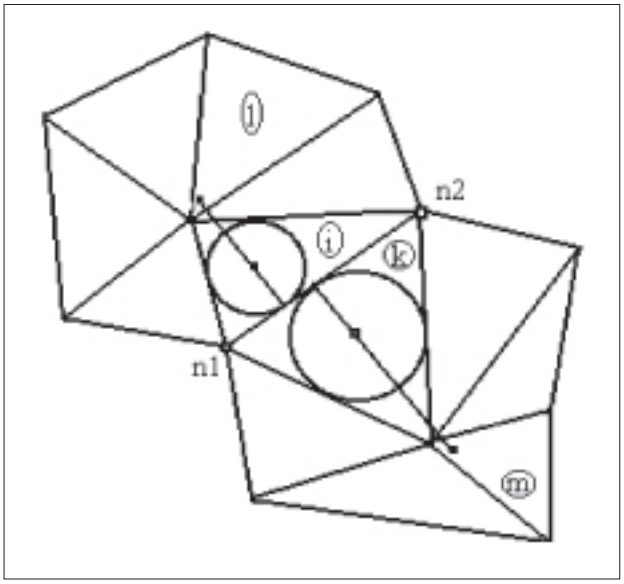

Figure 1: Sketch of the extrapolation stencil used for primitive variable linear reconstruction in the 2nd-order upwind schemes.

With the procedure just described, the state variables are represented as piecewise linear within each cell, instead of piecewise constant. But even considering a 2nd-order flux vector splitting scheme with a MUSCL approach, it is possible to obtain oscillations in the solution. Therefore one must use nonlinear corrections, namely limiters, to avoid any oscillations. In the present case, a simple minmod

limiter (Hirsch, 1990) is adopted. Previous experience (Azevedo and Figueira da Silva, 1997) with other limiters, such as the van Leer, van Albada and superbee limiters have indicated that these may not reach machine zero convergence in some cases. On the other hand, the minmod limiter was always able to drive convergence to machine zero in the cases tested in Azevedo and Figueira da Silva (1997) and it was, therefore, the limiter chosen for the present study. In order to obtain the expression for the limiter, one has to compute the ratios of consecutive variations. The limiter will be defined as a function of these ratios. Hence, if one defines

$$\begin{aligned} r^-(\xi,\eta,\zeta,w) &= \frac{\zeta-\xi}{\xi-\eta}\,, \\ r^+(\xi,\eta,\zeta,w) &= \frac{\zeta-\xi}{w-\zeta}, \end{aligned} \tag{21}$$

the limiters, which will be denoted by ϕ^- and ϕ^+ , can be written in the minmod case as

$$\phi^{\pm} = \phi(r^{\pm}) = \begin{cases} \min(r^{\pm},1) & \text{, if } r^{\pm}>0, \\ 0 & \text{, otherwise.} \end{cases} \tag{22}$$

With the previous definitions, the left and right states at the interface can be written as:

for the $E^{\pm}$ flux,

$$\begin{aligned} \Delta y_{ik} \geq 0 \;\Rightarrow\; & \begin{cases} W_L = \mathcal{F}^-(W_i, W_\ell, W_k, W_m) \\ W_R = \mathcal{F}^+(W_k, W_m, W_i, W_\ell) \end{cases} \\ \Delta y_{ik} < 0 \;\Rightarrow\; & \begin{cases} W_L = \mathcal{F}^-(W_k, W_m, W_i, W_\ell) \\ W_R = \mathcal{F}^+(W_i, W_\ell, W_k, W_m) \end{cases} \end{aligned}$$

for the $F^{\pm}$ flux,

$$\begin{aligned} \Delta x_{ik} \leq 0 \;\Rightarrow\; & \begin{cases} W_L = \mathcal{F}^-(W_i, W_\ell, W_k, W_m) \\ W_R = \mathcal{F}^+(W_k, W_m, W_i, W_\ell) \end{cases} \\ \Delta x_{ik} > 0 \;\Rightarrow\; & \begin{cases} W_L = \mathcal{F}^-(W_k, W_m, W_i, W_\ell) \\ W_R = \mathcal{F}^+(W_i, W_\ell, W_k, W_m) \end{cases} \end{aligned} \tag{23}$$

The functions F^- and F^+ reconstruct, respectively, the W_L and W_R states, and they are given by

$$\begin{aligned} \mathcal{F}^-(\xi,\eta,\zeta,w) &= \xi + \frac{\phi^-}{2}(\xi-\eta)\,, \\ \mathcal{F}^+(\xi,\eta,\zeta,w) &= \zeta - \frac{\phi^+}{2}(w-\zeta), \end{aligned} \tag{24}$$

where ϕ^- and ϕ^+ are the limiters previously defined.

First-and Second-Order Liou Schemes

The Liou schemes implemented in this work consider that the convective operator can be expressed as a sum of the convective and pressure terms (Liou, 1994, and Liou, 1996). The inviscid flux vectors can be written as

$$\begin{aligned} E &= u\Phi + P_x = M_x\, a\, \Phi + P_x\,, \\ F &= v\Phi + P_y = M_y\, a\, \Phi + P_y\,, \end{aligned} \tag{25}$$

where the Φ, P_x and P_y vectors are defined as

$$\Phi = \begin{Bmatrix} \rho \\ \rho u \\ \rho v \\ \rho H \end{Bmatrix} \qquad P_x = \begin{Bmatrix} 0 \\ p \\ 0 \\ 0 \end{Bmatrix} \qquad P_y = \begin{Bmatrix} 0 \\ 0 \\ p \\ 0 \end{Bmatrix}. \tag{26}$$

In the previous expressions, p is the pressure, H is the total specific enthalpy, $M_x = u/a$, and $M_y = v/a$.

The approach followed in the present work in order to extend Liou's ideas (Liou, 1994) to the unstructured grid case consists of defining a local one-dimensional stencil normal to the edge considered. The reason for this can be perceived if one observes, based on Eq. (17), that the contribution of the ik edge to the convective operator can be written as

$$\begin{aligned} \text{contrib. of } ik \text{ edge} &= E_{ik}\,\Delta y_{ik} - F_{ik}\,\Delta x_{ik} \\ &= (E_{ik}\, n_{x_{ik}} + F_{ik}\, n_{y_{ik}})\,\ell_{ik} \end{aligned} \tag{27}$$

where the normal $\vec{n}_{ik}$ to the ik edge, positive outwards with respect to the i-th triangle, is defined as

$$\vec{n}_{ik} = n_{x_{ik}}\,\hat{\imath} + n_{y_{ik}}\,\hat{\jmath} = \frac{\Delta y_{ik}}{\ell_{ik}}\,\hat{\imath} - \frac{\Delta x_{ik}}{\ell_{ik}}\,\hat{\jmath}\,. \tag{28}$$

Here, ℓ_{ik} is the length of the ik edge. Hence, one can write

$$\text{contribution of } ik \text{ edge} = \left(F_{ik}^{(c)} + P_{ik}\right)\ell_{ik}\,. \tag{29}$$

where, for now, it is sufficient to write $F_{ik}^{(c)}$ and P_{ik} as

$$\begin{aligned} F_{ik}^{(c)} &= (u\, n_x\, \Phi + v\, n_y\, \Phi)_{ik}\,, \\ P_{ik} &= (P_x\, n_x + P_y\, n_y)_{ik} = p_{ik} \begin{Bmatrix} 0 \\ n_{x_{ik}} \\ n_{y_{ik}} \\ 0 \end{Bmatrix}. \end{aligned} \tag{30}$$

For the construction of the first-order scheme, one must identify the "left" (or L) state, as defined in Liou (1994, 1996), as the properties of the i-th triangle and the "right" (or R) state as those of the k-th triangle (see Fig. 1 for the geometry definition). Hence, the interface Mach number, M_{ik}, also according to the definition in Liou (1994, 1996), can be written as

$$M_{ik} = M_L^+ + M_R^-\,, \tag{31}$$

where $M_L^+ = M^+(M_L)$ and $M_R^- = M^-(M_R)$. The split Mach numbers are defined as

$$M_L^+ = \begin{cases} \frac{1}{2}\left(M_L + |M_L|\right) & \text{, if } |M_L| \geq 1\,, \\ M_\beta^+(M_L) & \text{, otherwise,} \end{cases} \tag{32}$$

and, similarly,

$$M_R^- = \begin{cases} \frac{1}{2}\left(M_R - |M_R|\right) & \text{, if } |M_R| \geq 1\,, \\ M_\beta^-(M_R) & \text{, otherwise.} \end{cases} \tag{33}$$

The $M_\beta^{\pm}$ terms can be written as

$$M_\beta^{\pm}(M) \;=\; \pm\frac{1}{4}(M \pm 1)^2 \;\pm\; \beta(M^2-1)^2\,. \tag{34}$$

The present work used $\beta = 1/8$, as suggested in Liou (1994). Moreover, in order to achieve a unique splitting in Liou's sense, the left and right Mach numbers are defined as

$$M_L = \frac{\tilde{V}_L}{a_{ik}} \quad \text{and} \quad M_R = \frac{\tilde{V}_R}{a_{ik}}\,, \tag{35}$$

where

$$\begin{aligned} \tilde{V}_L &= u_L\, n_{x_{ik}} + v_L\, n_{y_{ik}}\,, \\ \tilde{V}_R &= u_R\, n_{x_{ik}} + v_R\, n_{y_{ik}}\,. \end{aligned} \tag{36}$$

The corresponding speed of sound, a_{ik}, at the interface is given by

$$a_{ik} = \min\left(\tilde{a}_L\,,\, \tilde{a}_R\right), \tag{37}$$

where

$$\begin{aligned} \tilde{a}_L &= a_L^* \cdot \min\left(1\,,\, \frac{a_L^*}{\left|\tilde{V}_L\right|}\right), \\ a_L^* &= \sqrt{\frac{2(\gamma-1)}{(\gamma+1)}\,H_L}\,, \end{aligned} \tag{38}$$

and a similar definition for $\tilde{a}_R$. The pressure, p_{ik}, at the ik interface is given by

$$p_{ik} \;=\; p_L^+\, p_L \;+\; p_R^-\, p_R\,. \tag{39}$$

The split pressures, still following the expressions in Liou (1994, 1996), can be written as

$$p_L^+ = \begin{cases} \frac{1}{2}\left(1 + \text{sign}(M_L)\right) & \text{, if } |M_L| \geq 1\,, \\ p_\alpha^+(M_L) & \text{, otherwise,} \end{cases} \tag{40}$$

and, similarly,

$$p_R^- = \begin{cases} \frac{1}{2}\left(1 - \text{sign}(M_R)\right) & \text{, if } |M_R| \geq 1\,, \\ p_\alpha^-(M_R) & \text{, otherwise.} \end{cases} \tag{41}$$

The $p_\alpha^{\pm}$ terms can be written as

$$p_\alpha^{\pm}(M) \;=\; \frac{1}{4}(M \pm 1)^2(2 \mp M) \;\pm\; \alpha M(M^2-1)^2\,. \tag{42}$$

This work used $\alpha = 3/16$, as suggested in Liou (1994). The convective operator, as defined in Eq. (17), can be finally written as

$$C(Q_i) \;=\; \sum_{k=1}^{3}\left[\left(F_{ik}^{(c)} + P_{ik}\right)\ell_{ik}\right], \tag{43}$$

where

$$F_{ik}^{(c)} \;=\; \frac{1}{2}\,M_{ik}\,a_{ik}\left(\Phi_L + \Phi_R\right) \;-\; \frac{1}{2}\,|M_{ik}|\,a_{ik}\left(\Phi_R - \Phi_L\right) \tag{44}$$

and P_{ik} has already been defined in Eq. (30). The second order scheme follows exactly the same formulation, except that the left and right states are obtained by a MUSCL extrapolation of primitive variables as described in the previous section. Therefore, the left state is defined by a limited extrapolation of the properties in the *i*-th and *l*-th triangles, and the right state is defined by a limited extrapolation of the properties in the *k*-th and *m*-th triangles. The minmod limiter was again used in this case.

TIME DISCRETIZATION

The Euler equations, fully discretized in space and assuming a stationary mesh, can be written as

$$\frac{dQ_i}{dt} = -\frac{1}{V_i}\left[C(Q_i) - D(Q_i)\right], \tag{45}$$

where the $D(Q_i)$ operator is identically zero if an upwind spatial discretization is used. The present work uses a fully explicit, 2nd-order accurate, 5-stage Runge-Kutta time-stepping scheme (Mavriplis, 1988) to advance the solution of the governing equations in time. The time integration scheme can, therefore, be written as

$$\begin{aligned} Q_i^{(0)} &= Q_i^n\,, \\ Q_i^{(1)} &= Q_i^{(0)} - \alpha_1\frac{\Delta t_i}{V_i}\left[C\left(Q_i^{(0)}\right) - D\left(Q_i^{(0)}\right)\right]\,, \\ Q_i^{(2)} &= Q_i^{(0)} - \alpha_2\frac{\Delta t_i}{V_i}\left[C\left(Q_i^{(1)}\right) - D\left(Q_i^{(1)}\right)\right]\,, \\ &\vdots \quad\quad \vdots \\ Q_i^{(5)} &= Q_i^{(0)} - \alpha_5\frac{\Delta t_i}{V_i}\left[C\left(Q_i^{(4)}\right) - D\left(Q_i^{(1)}\right)\right]\,, \\ Q_i^{n+1} &= Q_i^{(5)}\,, \end{aligned} \tag{46}$$

where the superscripts *n* and *n + 1* indicate that these are property values at the beginning and at the end of the *n*-th time step. The values used for the α coefficients were

$$\alpha_1 = \frac{1}{4}\,,\; \alpha_2 = \frac{1}{6}\,,\; \alpha_3 = \frac{3}{8}\,,\; \alpha_4 = \frac{1}{2}\,,\; \alpha_5 = 1\,. \tag{47}$$

It should be observed that the convective operator, $C(Q)$, is evaluated at every stage of the integration process, but the artificial dissipation operator, $D(Q)$, is only evaluated at the two initial stages (and, obviously, only for the central difference scheme). For steady-state problems, a local time stepping option has been implemented

in order to accelerate convergence. The details of the implementation of the variable time step option can be found in Azevedo and Figueira da Silva (1997).

DATA STRUCTURES

In a cell-centered finite volume context, the standard procedure for flux calculation consists of a loop over the control volumes which adds up the contribution of each edge, or side, to form the flux balance for that particular volume. This is usually called a volume-based data structure, which is the equivalent in the present case of an element-based data structure for the finite element community. Although "natural" and straightforward to implement, this procedure is not the most efficient because fluxes end up being computed twice for each edge of the control volume. For an explicit scheme, this means that the code could theoretically run twice as fast simply by implementing some procedure that would avoid recomputing the fluxes for the same edge.

One of the possibilities for solving this problem is to implement a so-called edge-based (or side-based) data structure (Mavriplis, 1988). In this case, the idea is to index the code computations based on the control volume edges. The discussion presented here considers a triangular unstructured grid. However, a similar procedure could be implemented regardless of the type of control volume used. The connectivity information for a cell-centered finite volume algorithm on a volume-based data structure consists of two major "tables." The first one indicates, for each triangle, the nodes of the mesh which form the triangle. The other table points to the three triangles which are neighbors of the particular triangle considered. For an edge-based data structure, the connectivity information is centered on the edges and, for each edge, enough information should be stored to allow the necessary computations over the complete grid.

In the present work, since a cell-centered scheme is being used, the following procedure is adopted:

For each edges store: (n_1, n_2, i, k) . (48)

Here, n_1 and n_2 are the two nodes which define the edge, i is the triangle to the left of the $\overline{n_1 n_2}$ segment, and k is the triangle to the right of it (see Fig. 1 for details). Moreover, the $\overline{n_1 n_2}$ segment is assumed to be oriented from n_1 to n_2 . This notion of orientation of a segment is fundamental to the algorithm because, with the present implementation, the nodes n_1 and n_2 are arranged in a counterclockwise fashion for the i-th control volume and in a clockwise fashion for the k-th control volume. Therefore, the flux computed for this particular edge is added to the flux balance equation of the i-th control volume and subtracted from that of the k-th control volume. Hence, for an edge-based data structure, the main loop runs over edges, or sides, and the contribution of the side to the neighboring control volumes is computed and added (or subtracted) to (from) that volume's flux balance equation.

The previous information would be enough for the centered scheme and for the first-order upwind schemes implemented here. However, as already discussed, further information is necessary in order to implement the second-order versions of the upwind schemes. For the second-order upwind schemes, the edge-based information stored must be augmented in order to also include the identification of the two additional triangles which are used for the linear reconstruction process. Hence, using the nomenclature previously defined, one should:

For each edges store: (n_1, n_2, i, k, l, m) . (49)

The procedure used to define triangles l and m has already been previously described in the paper. The search operations necessary to identify these triangles are performed at a pre-processing stage, such that the computational cost associated with this search is negligible in the overall solution cost. It should be emphasized that this identification must also be performed after each adaptive refinement pass, since the complete connectivity information is updated in the refinement process.

ADAPTIVE GRID REFINEMENT

The concept behind using an adaptive mesh strategy is to refine regions where large gradients occur. For many problems, the regions that need to be refined are small compared with the size of the complete computational domain. Therefore, one can reduce storage and CPU requirements by the use of adaptive refinement, when compared with a fixed fine mesh which would yield the same resolution of the relevant flow features. In order to identify the regions that require grid refinement, a sensor must be defined. The sensor used in this work is based on gradients of flow properties. Its general definition could be expressed as

$$(\text{sensor})_i = \left\{ \max_n \left[\frac{|\nabla \phi_n|}{\left| \phi_{n\max} - \phi_{n\min} \right|} \right] \right\}_i , \quad \text{where} \quad \phi_n = (\rho, p, u, v, T) \ , \tag{50}$$

and ϕ_{nmax} and ϕ_{nmin} are the maximum and the minimum values of the ϕ_n property in the flowfield. Despite this general definition, and despite having implemented the complete sensor calculation as indicated in the above

equation, all results presented in this work have used a sensor based on density gradients, i.e., $\phi_n = \rho$.

The first step of the adaptive procedure is to compute the flow on an existing coarse mesh. With this preliminary solution, one can calculate the sensor as previously described. The code marks all triangles in which the sensor exceeds some specified threshold value (the threshold value will be denoted Γ in the present paper), and the marked triangles are refined. A new finer mesh is then constructed by enrichment of the original coarse grid.

The mesh enrichment procedure consists of introducing an additional node for each side of a triangle marked for refinement. For interior sides, this additional node is placed at the mid-point of the side whereas, for boundary sides, it is necessary to refer to the boundary definition to ensure that the new node is placed on the true boundary. After this initial pass, the code has to search all triangles to identify cells that have two or three divided sides. Each of these cells is subdivided into four new triangles. This subdivision may eventually mark new faces. Therefore, this process has to be performed until there are no triangles with more than one marked face. In order to avoid hanging nodes, the triangles that have one marked face should be divided by halving. Figure 2 illustrates the three possible ways of triangle subdivision.

The second part of the refinement process consists of identifying all triangles which were refined by halving. This information is stored for the next refinement step because, if there is again an attempt to subdivide these triangles by halving, this is not allowed. Experience has shown that repeated triangle division by halving has a strong detrimental effect in mesh quality. Therefore, if the next refinement step tries to divide by halving a triangle which was obtained by halving from a previous division, the logic in the code forces the original triangle to be divided into four new triangles before the refinement procedure is allowed to continue. When the mesh enrichment procedure has been completed, the new control volumes receive the property values of their "father" triangle and the flow solver is re-started.

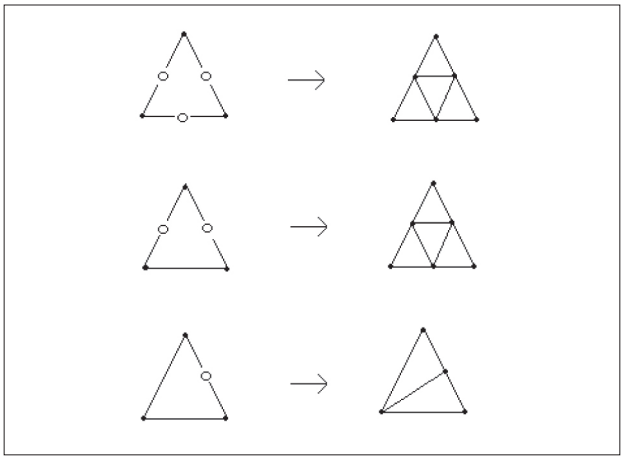

Figure 2: Schematic representation of the three possible triangle subdivision processes.

RESULTS AND DISCUSSION

A 2-D inlet configuration which is representative of some proposed inlet geometries for a typical transatmospheric vehicle was used as a test in the present work. To analyze the different schemes, an adaptive mesh and both a coarse and a fine fixed unstructured meshes were used. In the present work, the expression "fixed" mesh will denote a grid which was generated as close as possible to an equally spaced mesh in the unstructured context. Therefore, the expression "fixed grid" is being used here in opposition to the expression "adaptively refined" grid. The adaptive mesh was obtained with 3 passes of refinement using the 1st-order Liou scheme as the flow solver. The adaptive refinement process described in the previous section was used and the sensor was based on density gradients. The initial mesh had 399 nodes and 683 triangles. The successive refinement passes used threshold values Γ =(0.005, 0.005, 0.005). This mesh ended up with 11152 nodes and 21692 volumes. The initial mesh and the two intermediate meshes in this process are shown in Fig. 3. In the present case, 500 iterations were performed before the first refinement pass, 800 iterations between the first and the second ones, and 1200 iterations between the second and the third refinement passes. This represents a typical pattern observed in the present study

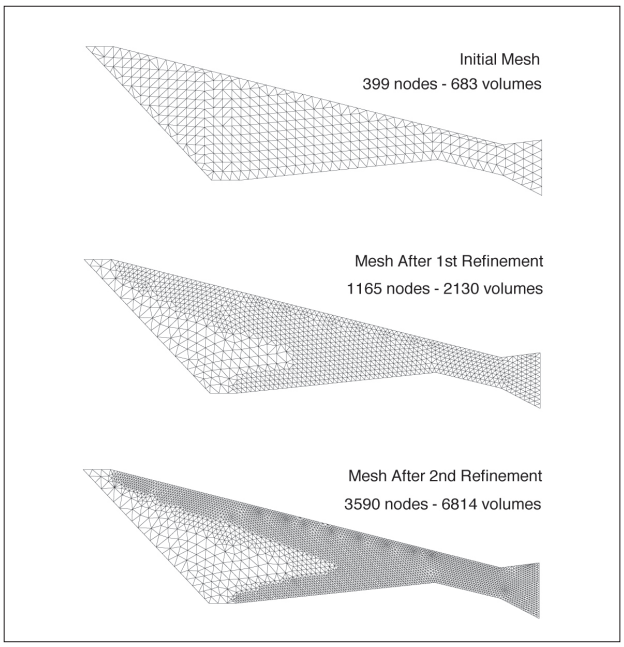

Figure 3: Initial and intermediate grids in the adaptive refinement procedure.

in the sense that the optimal number of iterations between successive refinement passes increases as the grid is refined. The final mesh is shown as the bottom plot in Fig. 4. This is the adaptively refined grid which was used for comparison of the various schemes in the paper.

The coarse fixed grid had 4204 nodes and 8006 volumes. Results for coarser grids were also obtained, but these results were deemed either excessively poor for the purpose of the present comparisons or of comparable resolution with the ones obtained with the above referred grid. A fine fixed mesh was also generated and this grid had 12005 nodes and 23324 triangles. The major requirement in the generation of this fine fixed grid was to have an essentially equally spaced mesh with the number of nodes, or triangles, comparable to those of the final adaptively refined grid. Therefore, the three different meshes used in the calculations and comparisons, which are reported here, are presented in Fig. 4. The coarse fixed mesh is seen as the top plot in Fig. 4, the fine mesh is the middle one and the adaptively refined grid is the bottom plot in this figure.

For the present simulations, the fluid was treated as a perfect gas with constant specific heat and no chemistry was taken into account. The purpose of these simulations is to compare the different schemes applied to high Mach number flows in order to verify if they are able to represent all flow features, such as strong shocks, shock reflections and interactions, and expansion regions. Moreover, there is interest in verifying whether the schemes can avoid oscillations in the presence of such strong discontinuities.

The results considering an inlet entrance Mach number M_∞ = 12 are discussed in detail in the paper. The Mach contours obtained with the five schemes are presented in Figs. 5–9 for the calculations with the coarse fixed mesh. The figures present, respectively, the results with the centered scheme, the 1st- and 2nd-order van Leer flux-vector splitting schemes and the 1st- and 2nd-order Liou AUSM$^+$ schemes. The contours indicate that the overall flow features are well captured by all solutions, at least in the upstream portion of the inlet. However, they also suggest that, at least with this coarse fixed mesh, all schemes produce oscillations in the solution. The oscillations are more evident in the results with the centered scheme, as one might expect. Nevertheless, the somewhat ragged contours for the both upper and lower wall entrance shocks for all calculations are an indication that there are oscillations in these solutions. Moreover, the Mach number contours shown in Figs. 5–9 also indicate that the resolution of flow features downstream of the interaction region of the two entrance shocks is not very good with this coarse mesh. Essentially, one cannot see much of the shock reflections and expansions that should be present in these downstream regions.

A summary of the analysis of these figures indicates that the entrance flow features are well captured by the centered scheme, as already discussed, except that one can clearly see the oscillations upstream of the strong upper wall entrance shock. One can see in Figs. 6 and 8 that the 1st-order van Leer and 1st-order Liou schemes smooth out the spatial gradients by the intrinsic artificial dissipation present in these schemes, which is typical of 1st-order upwind discretizations. Moreover, the 2nd-order schemes implemented in this work presented a better shock-capturing capability compared with the other schemes. They do not have as much shock-smearing as their 1st-order versions and, at the same time, they do not present as much evidence of solution oscillation as the 2nd-order centered scheme. Unfortunately, as discussions

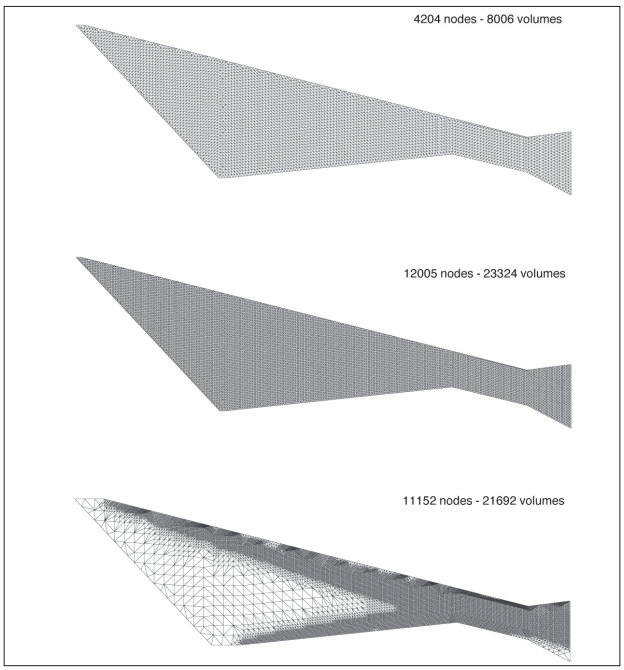

Figure 4: Complete view of the three computational meshes used in the present comparisons: (a) coarse fixed mesh; (b) fine fixed mesh; and (c) adaptive mesh.

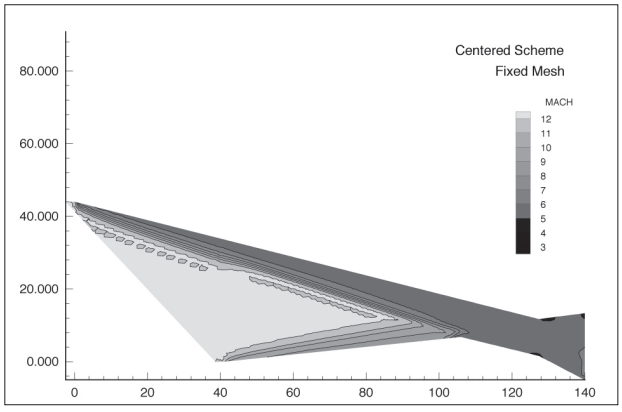

Figure 5: Mach number contours obtained with the coarse fixed mesh for the centered scheme (M_∞ = 12).

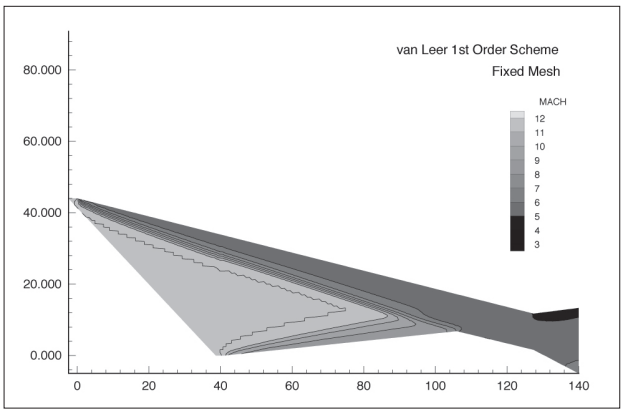

Figure 6: Mach number contours obtained with the coarse fixed mesh for the 1st-order van Leer scheme ($M_\infty = 12$).

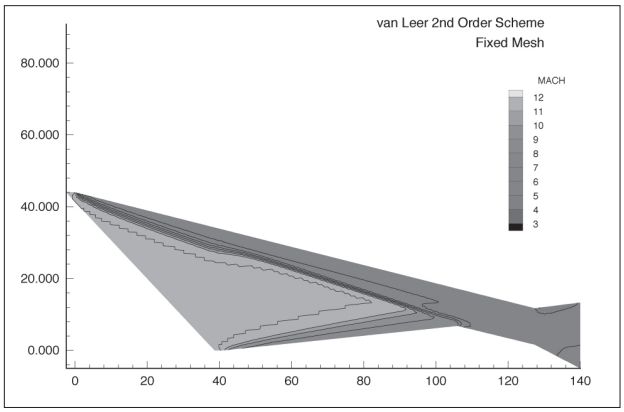

Figure 7: Mach number contours obtained with the coarse fixed mesh for the 2nd-order van Leer scheme ($M_\infty = 12$).

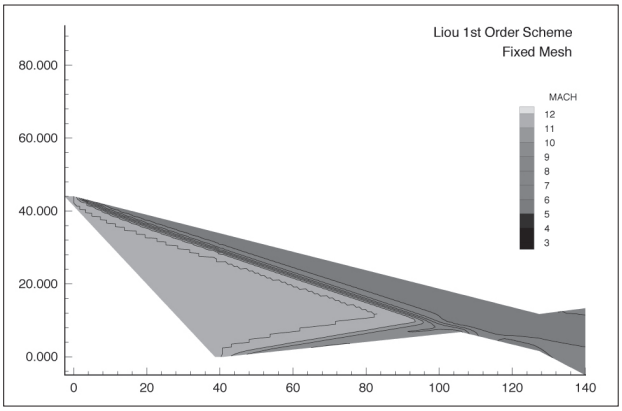

Figure 8: Mach number contours obtained with the coarse fixed mesh for the 1st-order Liou scheme ($M_\infty = 12$).

later in this paper will show, only the analysis of the Mach number contours can be misleading as far as an overall study of solution oscillations is concerned.

Corresponding results for the fine fixed grid are shown in Figs. 10–14. These again consider an entrance Mach number $M_\infty = 12$ and calculations with the five discretization schemes are represented in these figures. The first aspect which is clearly evident from the figures is that the upstream entrance shocks are much better defined in the finer grid solution. Moreover, some of the downstream flow features, which could not be seen in the coarse grid solution, are now starting to become apparent in the fine grid. However, the grid resolution in the downstream portions of the flow is clearly still not sufficient to resolve all details of the flowfield in these regions, especially for the more dissipative 1st-order schemes.

The oscillations in the upper wall entrance shock for the centered scheme solution are also quite visible in this fine fixed grid solution, as shown in Fig. 10. These oscillations are restricted to a narrower region of the flow, as one should expect due to the increased mesh refinement, but they are still present in the solution. Moreover, oscillations in the lower wall entrance shock can also be seen in Fig. 10. The definition of the entrance shocks in the upwind solutions is improved with the current grid, both for the 1st- and the 2nd-order schemes. This improvement is consistent with the one observed for the centered scheme case. However, one can observe some sort of an inflection in the upper wall entrance shock for the 2nd-order van Leer flux-vector splitting scheme solution (see Fig. 12), which clearly does not have any physical meaning. Actually, it is possible to see a similar problem in the coarse grid solution with this scheme, shown in Fig. 7. The problem, however, becomes even more evident in the fine grid result shown in Fig. 12. A close inspection of the Mach number contours obtained with the 2nd-order AUSM$^+$ scheme also reveals a similar inflection problem in the upper wall entrance shock. As one can see in Fig. 14, however, this spurious behavior is much less pronounced in the solution with the 2nd-order Liou scheme.

Despite the clear improvement in flow feature resolution provided by the finer fixed mesh, as already pointed out, an overall assessment of the previous results indicates that some aspects of the flow are still very poorly resolved even with this fine grid. In particular, one can observe that the lower wall entrance shock is quite smeared and that the downstream portions of the flow are not adequately resolved. Hence, the use of an adaptively refined mesh seemed to be the best approach in order to allow the grid density to be driven by the solution itself. The corresponding Mach number contours for freestream Mach number $M_\infty = 12$, computed with the final adaptively refined mesh, are shown in Figs. 15–19. In general, these results indicate a much sharper definition of both upper and lower wall entrance shocks and of the flow features downstream of the shock interaction region. Although the full resolution of this interaction may still require further grid refinement, the results in Figs. 15–19 can already provide an idea of the flow structure in the downstream portions of the configuration.

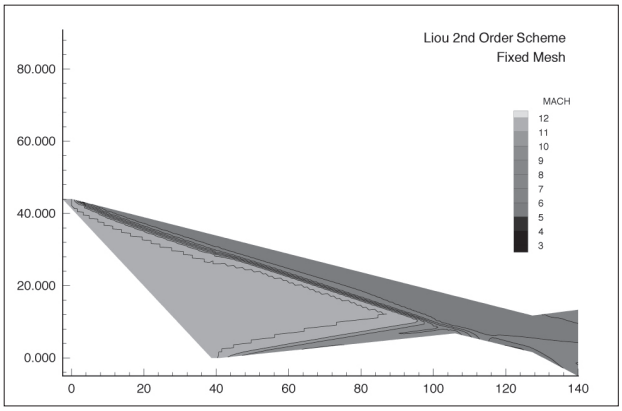

Figure 9: Mach number contours obtained with the coarse fixed mesh for the 2nd-order Liou scheme ($M_\infty = 12$).

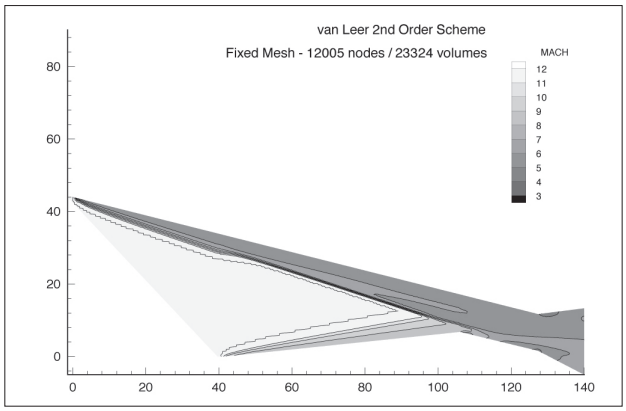

Figure 12: Mach number contours obtained with the fine fixed mesh for the 2nd-order van Leer scheme ($M_\infty = 12$).

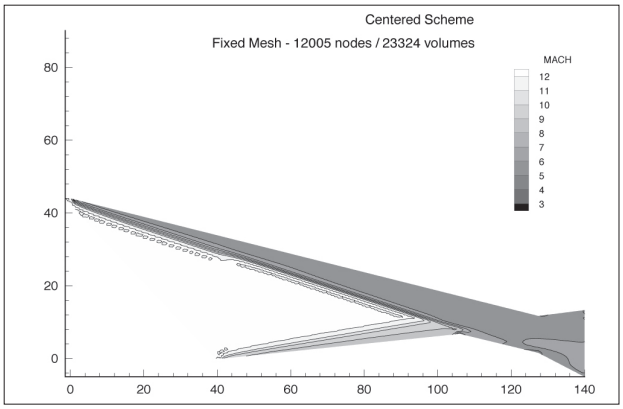

Figure 10: Mach number contours obtained with the fine fixed mesh for the centered scheme ($M_\infty = 12$).

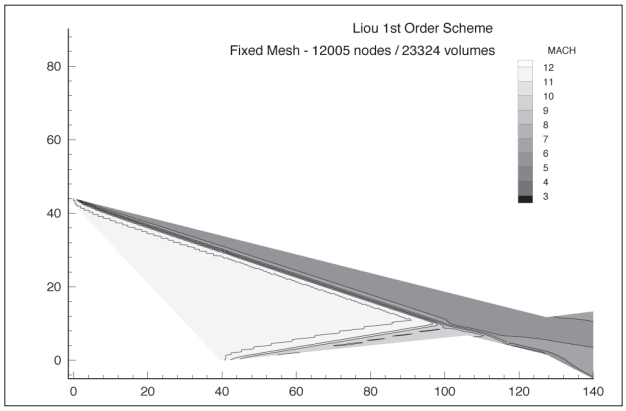

Figure 13: Mach number contours obtained with the fine fixed mesh for the 1st-order Liou scheme ($M_\infty = 12$).

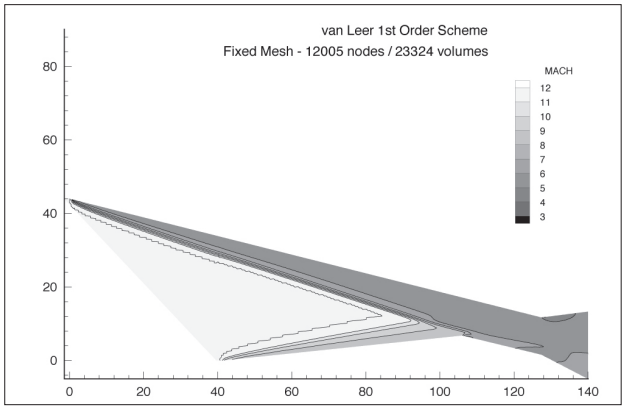

Figure 11: Mach number contours obtained with the fine fixed mesh for the 1st-order van Leer scheme ($M_\infty = 12$).

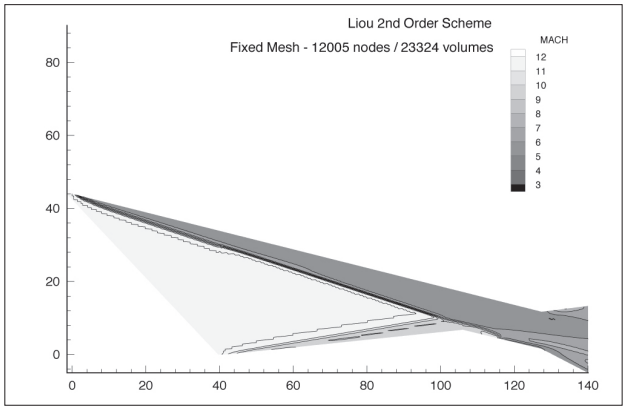

Figure 14: Mach number contours obtained with the fine fixed mesh for the 2nd-order Liou scheme ($M_\infty = 12$).

One can see in Fig. 15 that the centered scheme still exhibits oscillations in this case, especially near the upper wall inlet lip. However, a comparison of Figs. 4 and 15 indicates that the oscillations mostly occur in a region in which the mesh is quite coarse, i.e., they are in a region upstream of the densely refined mesh area due to the presence of the upper wall shock. In any event, the centered scheme was not really expected to be able to cope with such strong shocks without oscillations. The Mach number contours for the calculations with the upwind schemes, however, also indicate the existence of oscillations in those solutions. For instance, the results

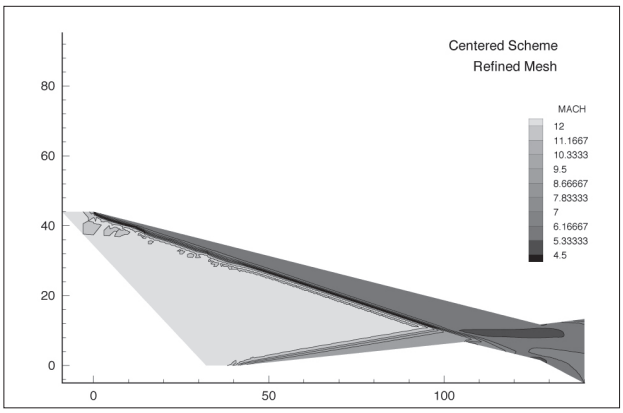

Figure 15: Mach number contours obtained with the adaptively refined mesh for the centered scheme ($M_\infty = 12$).

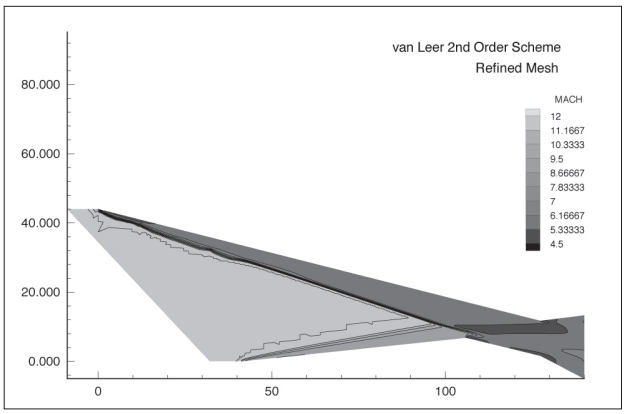

Figure 17: Mach number contours obtained with the adaptively refined mesh for the 2nd-order van Leer scheme ($M_\infty = 12$).

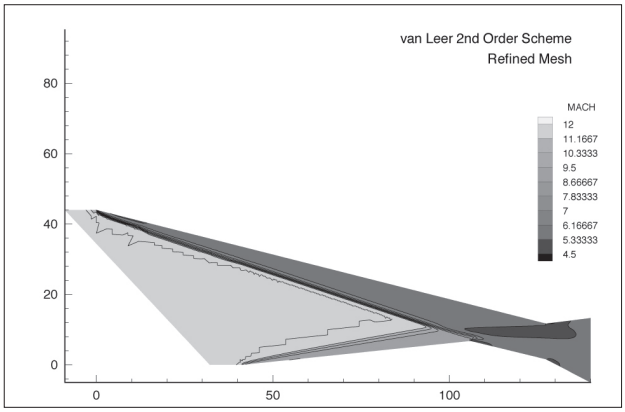

Figure 16: Mach number contours obtained with the adaptively refined mesh for the 1st-order van Leer scheme ($M_\infty = 12$).

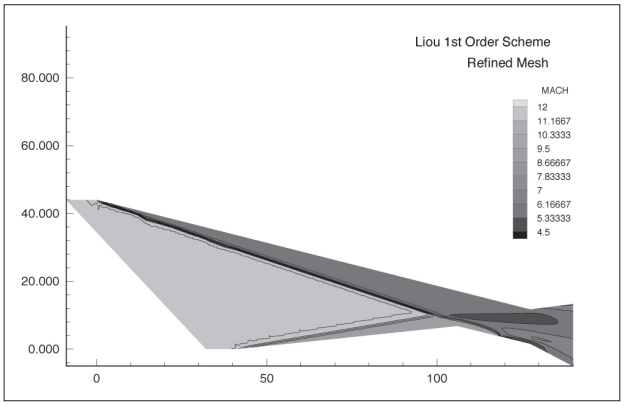

Figure 18: Mach number contours obtained with the adaptively refined mesh for the 1st-order Liou scheme ($M_\infty = 12$).

with both 1st- and 2nd-order versions of the van Leer scheme, shown in Figs. 16 and 17, present a rather ragged first contour in the entrance shock region. Moreover, both calculations also present considerable smearing of the weaker lower wall shock. Although, it is true that even this shock is much better defined by the adaptively refined grid solution with the two versions of van Leer's scheme than corresponding results with the other grids. The solutions with the van Leer schemes do not show much detail of the downstream portions of the flow. Again, one can see differences between the 1st- and 2nd-order results in this downstream region, but the scheme is clearly too diffusive despite the strong mesh refinement in the region.

An analysis based solely on the Mach number contours in Figs. 15–19 would indicate that the calculations with both versions of the AUSM$^+$ scheme yield the best resolution of flow features in this case. Furthermore, the 2nd-order results in Fig. 19 provide the best definition of both upper and lower wall entrance shocks, of the result of the shock-shock interaction and of the downstream expansion and compression regions. There are still indications of solution oscillations even for these results, especially near the upper wall inlet lip. However, they clearly provide the best overall description of the flow features among all schemes and different meshes analyzed. Unfortunately, as the forthcoming discussion will show, there are also serious problems with the Liou scheme solutions, both for the 1st- and 2nd-order versions of the scheme, which complicate the selection of a best overall result among the various tests performed.

Dimensionless pressure distributions along both the inlet upper and lower walls were also analyzed in order to obtain a better assessment of the solution quality for all test cases. As before, all cases consider an entrance Mach number $M_\infty = 12$. An initial comparison shows plots of pressure distributions, obtained with each one of the spatial discretization schemes studied, for all three meshes. The analytical solution for the inlet entrance region is also shown in each figure. This solution is correct up to the point in which structures resulting from

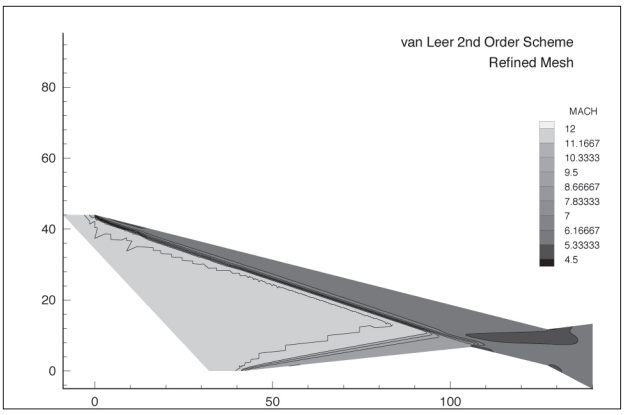

Figure 19: Mach number contours obtained with the adaptively refined mesh for the 2nd-order Liou scheme ($M_\infty = 12$).

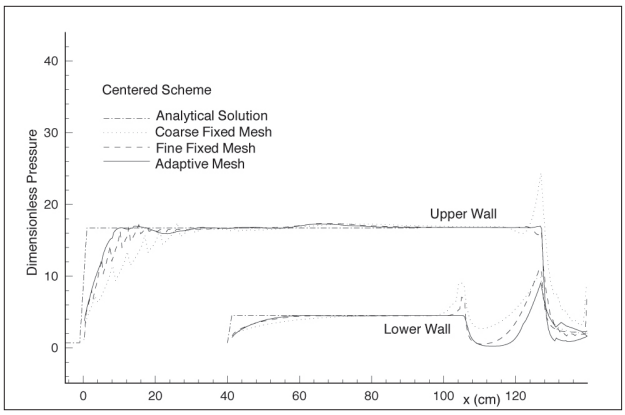

Figure 20: Analysis of the mesh effect in the wall pressure distributions obtained with the centered scheme ($M_\infty = 12$).

the shock-shock interaction start to impinge upon the inlet walls. Hence, Fig. 20 presents the dimensionless wall pressure distributions, for both upper and lower walls, obtained with the centered scheme. All calculations eventually reach the correct post-shock pressure plateaux, for both upper and lower walls. However, the numerical solutions approach their corresponding plateaux rather slowly, or over a fairly long longitudinal distance, and in a very oscillatory fashion for both fixed mesh solutions. The behavior of the pressure distribution obtained with the adaptive mesh is far less oscillatory. The curve for the coarse fixed mesh also presents a very distinctive pressure peak immediately upstream of the expansion corner in the upper wall. This is caused by a shock, resulting from the shock-shock interaction, which impinges upon the upper wall. This shock, however, cannot be seen in the Mach number contours shown in Fig. 5. In general, the results with the fine fixed grid and with the adaptive grid are similar for this case, except for the oscillations in the upper wall shock in the fixed grid solution, as already discussed.

The comparison of the results obtained with the two versions of the van Leer scheme is shown in Figs. 21 and 22, respectively for the 1st- and 2nd-order schemes. The pressure distributions in the upper wall shock are much less oscillatory in this case, especially for the 1st-order scheme solution. This is to be expected since this scheme is quite a bit more diffusive than the others tested here. Actually, the previous discussion has indicated that the van Leer scheme is more diffusive and, clearly, its 1st-order implementation is more diffusive than the 2nd-order one. The solution with the 2nd-order scheme again presents oscillations in this region of the flow for the coarse fixed grid. Aside from the problems already discussed in the previous case with regard to the entrance shocks, one can also observe that there are marked differences in the pressure distributions, obtained with the different meshes, in the downstream portion of the flow. This is true for both 1st- and 2nd-order cases, but it seems to be more pronounced in the 1st-order results. Moreover, the results with the 2nd-order version of the scheme are indicating a gentle oscillation in the upper wall pressure distributions at x ≅ 70 cm. This feature can be seen in the results for all three meshes with the 2nd-order van Leer scheme, although its spatial position is slightly different depending on the grid. Such oscillation is clearly incorrect, since the pressure must be constant in this region.

The results with the 1st-order and the 2nd-order Liou schemes are shown in Figs. 23 and 24. The most distinctive feature of these results is that, in both cases, the solutions have strong oscillations at the upper wall entrance shock. There are oscillations in the lower wall shock too, but these are mild compared with the ones observed in the upper wall case. It is interesting that the same extreme oscillations are observed both in the 1st-order results as well as in the 2nd-order ones. The adaptive grid calculations present the results with the smallest oscillations in this case. However, even such milder oscillations would still be considered unacceptable if the present flow solver capability were to be coupled to the equations describing the real gas effects present in practice for such applications. One can also observe that there is good agreement among the pressure distributions, obtained with the different meshes in this case, for the downstream portions of the flow. The agreement is not as good for the case of the coarse fixed mesh, but this mesh is too coarse to resolve flow features in the downstream region anyway, as already discussed. Moreover, Figs. 23 and 24 are showing pressure distributions in the downstream portions of the flow which are quite different from the ones obtained with the van Leer scheme (see Figs. 21 and 22).

Further analysis of the results can be accomplished by looking at essentially the same data shown in Figs. 20 to 24, but from a different perspective. Therefore, Figs. 25–

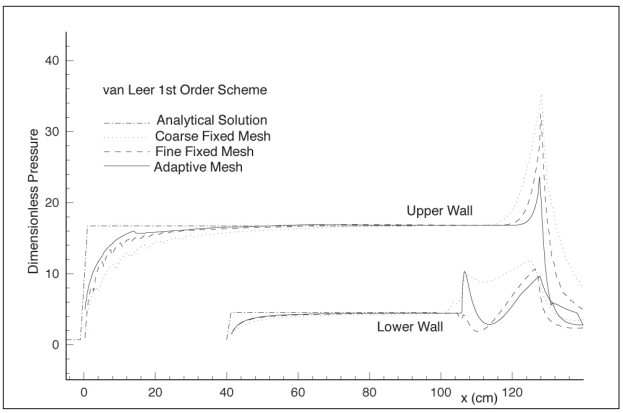

Figure 21: Analysis of the mesh effect in the wall pressure distributions obtained with the 1st-order van Leer scheme ($M_\infty = 12$).

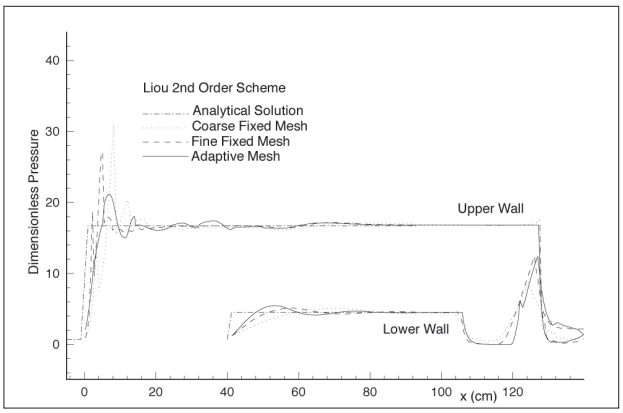

Figure 24: Analysis of the mesh effect in the wall pressure distributions obtained with the 2nd-order Liou scheme ($M_\infty = 12$).

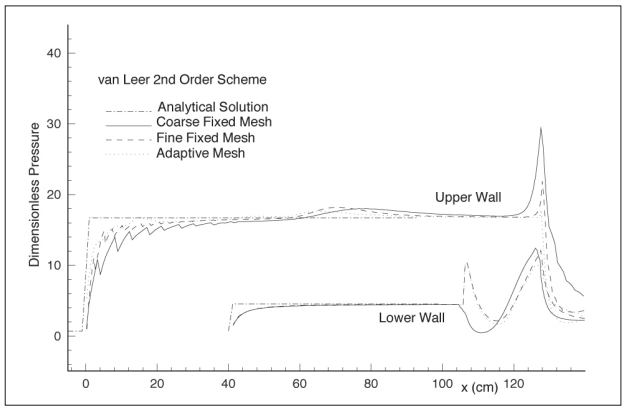

Figure 22: Analysis of the mesh effect in the wall pressure distributions obtained with the 2nd-order van Leer scheme ($M_\infty = 12$).

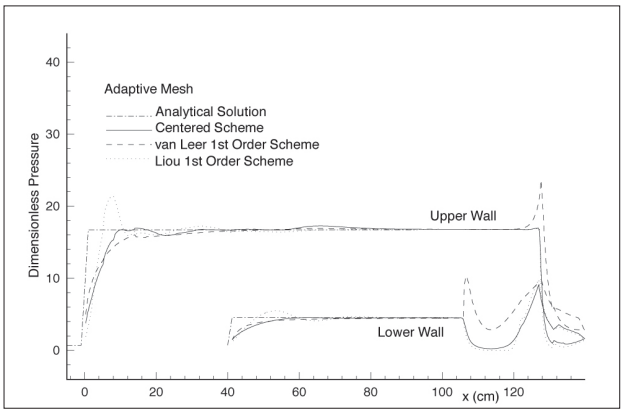

Figure 25: Analysis of the discretization scheme effect in the wall pressure distributions obtained for the adaptively refined grid ($M_\infty = 12$). Comparison of centered and 1st-order upwind schemes.

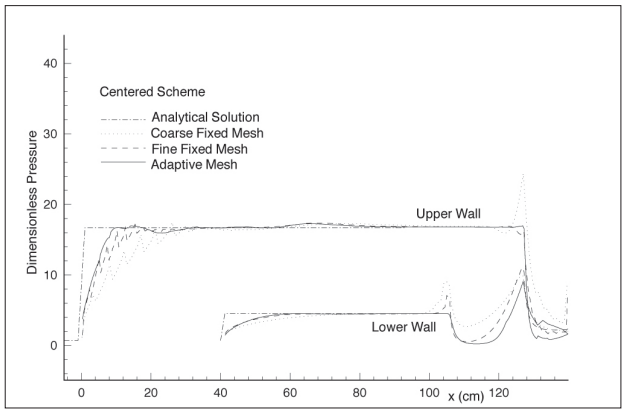

Figure 23: Analysis of the mesh effect in the wall pressure distributions obtained with the 1st-order Liou scheme ($M_\infty = 12$).

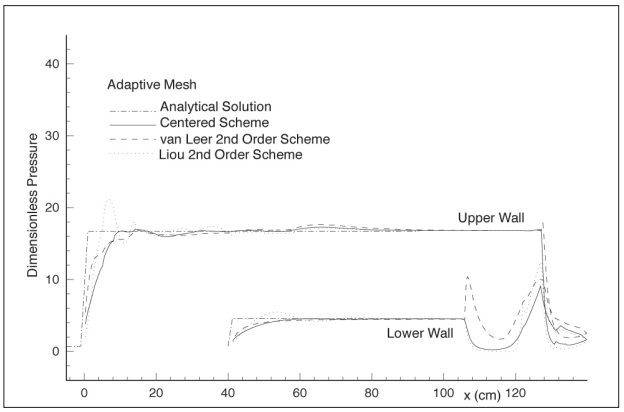

Figure 26: Analysis of the discretization scheme effect in the wall pressure distributions obtained for the adaptively refined grid ($M_\infty = 12$). Comparison of centered and 2nd-order upwind schemes.

28 allow for a more direct comparison of the discretization scheme effects on the solution, for a given mesh. As before, the dimensionless pressure distributions along the upper and lower inlet walls are being shown in these figures. The analytical solution for the pressure distribution along the upstream portion of both upper and lower inlet entrance walls is also shown for comparison purposes. The comparison in Fig. 25 includes the centered scheme and the two 1st-order upwind schemes, for solutions computed using the adaptively refined mesh. The analogous

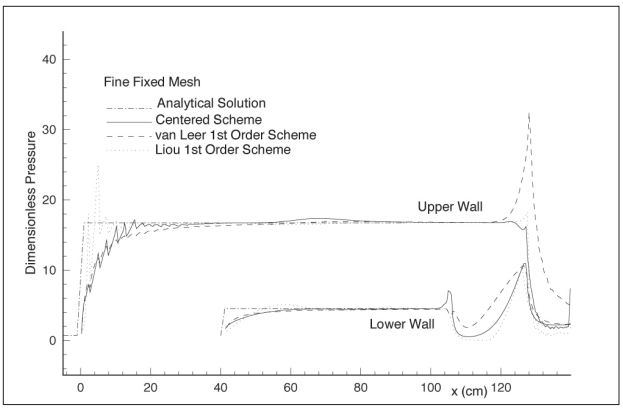

Figure 27: Analysis of the discretization scheme effect in the wall pressure distributions obtained for the fine fixed grid ($M_\infty = 12$). Comparison of centered and 1st-order upwind schemes.

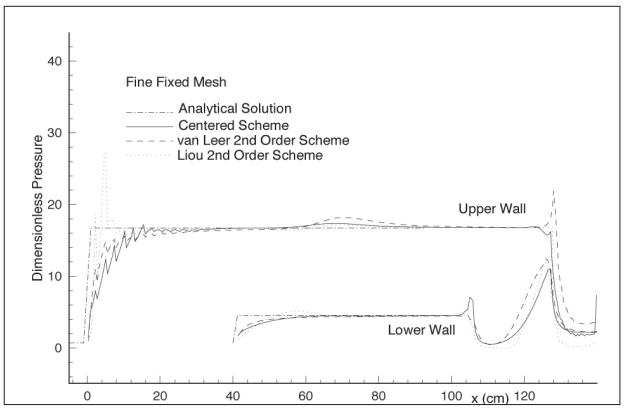

Figure 28: Analysis of the discretization scheme effect in the wall pressure distributions obtained for the fine fixed grid ($M_\infty = 12$). Comparison of centered and 2nd-order upwind schemes.

comparison including the two 2nd-order upwind schemes is presented in Fig. 26. Aside from some aspects which have already been discussed, such as the fact that the Liou scheme solutions are very oscillatory at the entrance shocks, one can state that, in general, there is a fairly good correlation between the results with the centered scheme and those with the AUSM$^+$ scheme. This is true for both 1st- and 2nd-order implementations of the Liou scheme.

On the other hand, the results with the van Leer scheme are quite different from the others downstream of the expansion corners on both upper and lower walls. Although these differences are also present in the 2nd-order van Leer solutions, the discrepancies are more evident in the 1st-order results. Essentially, the solution for the 1st-order implementation of the van Leer scheme seems to indicate that shock waves impinge on the upper and lower inlet walls approximately at the location of the wall expansion corners. For the lower wall, it would be more precise to state that the impingement would occur at the upstream expansion corner. The results with the other schemes do not corroborate this observation. They show no shock impingement at the inlet upper wall. In this case, even the 2nd-order van Leer solution does not show any shock impingement on the upper wall. Moreover, for the lower wall, both 1st- and 2nd-order van Leer solutions are fairly similar and, again, they are completely different from the wall pressure distributions obtained with the other schemes in this downstream flow region. Nevertheless, the wall pressure distributions obtained with the van Leer method indicate that this scheme is the most successful in preventing oscillations, among the algorithms tested, across the strong upper wall entrance shock. This is particularly true for the 1st-order version of the scheme.

A similar comparison is shown in Figs. 27 and 28 for the calculations performed with the fine fixed grid. The more relevant comments which can be made in this case are essentially equivalent to those already discussed in the context of the analysis of Figs. 25 and 26. In any event, it is interesting to observe that the pressure distributions obtained with the van Leer scheme are very similar to those calculated by the other schemes in this case, especially for the 2nd-order version of the method. The 1st-order van Leer results, particularly for the upper wall, are still quite different from the pressure distributions obtained with the other schemes. Unfortunately, the better correlation observed with the fine fixed grid can simply be the result of having a mesh which is too coarse in the downstream regions of the flow to actually capture the phenomena that should be present there.

Finally, pressure contours obtained with the adaptively refined mesh are shown in Figs. 29–31. These figures present, respectively, the contours for the solutions with the centered scheme, the 1st-order Liou scheme and the 2nd-order Liou scheme. The major objective of including these figures here is to provide further understanding of the flow features especially in the downstream regions. The pressure contours seem to be more revealing for the flow structures which appear downstream of the shock-shock interaction region. In general, the three solutions are quite similar in this case, as the previous discussions have already indicated. The more diffusive character of the 1st-order scheme is not as evident in Fig. 30, except for the thicker upper wall entrance shock. Pressure contours calculated with the fixed meshes (not shown here) would indicate that the additional numerical diffusivity of the 1st-order scheme would destroy some of the information in the downstream region. Moreover, it is also clear that the upper wall entrance shock is more sharply defined by the 2nd-order upwind solution than by either the centered or the 1st-order upwind calculations. The figures also seem to indicate that further refinement of the interaction region

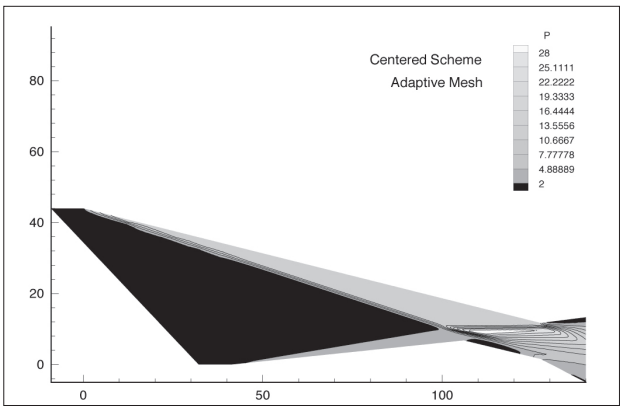

Figure 29: Dimensionless pressure contours obtained with the adaptively refined mesh for the centered scheme (M_∞ = 12).

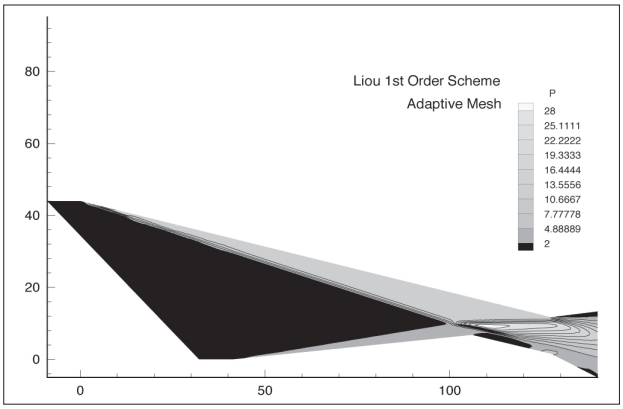

Figure 30: Dimensionless pressure contours obtained with the adaptively refined mesh for the 1st-order Liou scheme (M_∞ = 12).

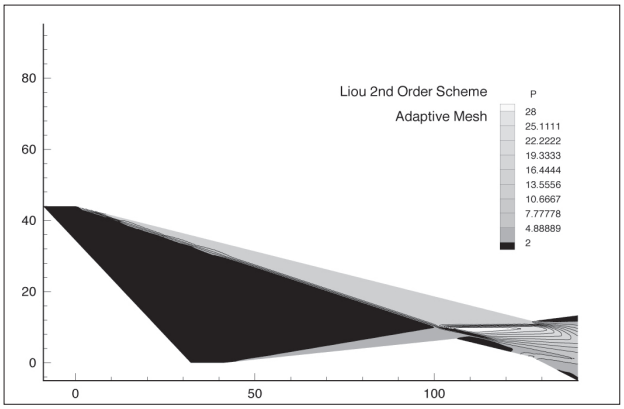

Figure 31: Dimensionless pressure contours obtained with the adaptively refined mesh for the 2nd-order Liou scheme (M_∞ = 12).

would still be necessary in order to fully characterize these downstream structures.

It is important to emphasize that similar calculations were performed for inlet entrance Mach numbers M_∞ = 4, 8 and 16, in the context of the present study. These results are not included here because the conclusions that can be drawn are essentially equivalent to those obtained with the M_∞ = 12 solution. As one could clearly expect, the oscillations observed in essentially all calculations here reported decrease as the inlet entrance Mach number is lowered. In a similar fashion, results for the M_∞ = 16 case are even more oscillatory than those here discussed.

Moreover, the authors would also like to emphasize that each case could be directly run with the adaptive refinement capability. This was not done in the present work because the final meshes, that would be obtained in such case, would be different since there are small differences in the converged solutions obtained with the various schemes. Therefore, the authors have chosen to compare the solutions obtained in a single mesh generated by an adaptive refinement procedure using one of the available spatial discretization schemes. Moreover, the most relevant comparisons in the present case must be those between the adaptively refined mesh results and the ones obtained with the fine fixed mesh, because these two meshes have approximately the same number of control volumes. As the results presented in the paper have demonstrated, the quality of the solutions obtained with the adaptive grid is certainly better, for the same computational cost.

Furthermore, it is also important to emphasize that, in actual flight, an inlet flow with entrance Mach number equal to 12, or 16, could not be simulated with the perfect gas assumption. In other words, real gas behavior would have to be taken into account. From a physical standpoint, however, the present calculations could be considered as the simulation of the cold gas flows which are usually achieved in experimental facilities such as gun tunnels. In order to extrapolate these results to actual flight conditions, dissociation and vibrational relaxation would certainly have to be included in the formulation. Nevertheless, the present simulations could be seen as a necessary step in the construction of a robust code to deal with the complete environment encountered in actual flight.

CONCLUDING REMARKS

The present work performed a comparison of five different spatial discretization schemes for cold gas hypersonic flow simulations. The schemes presented here were applied to the solution of supersonic and hypersonic inlet flows. The inlet entrance conditions were varied from M_∞ = 4 up to M_∞ = 16. An inviscid formulation was used and the fluid was treated as a perfect gas. Clearly, for actual flight condition simulation, real gas effects would have to be taken into account. Here, however, the consideration of very high Mach number flows simply has the objective of testing the behavior of the different schemes in the presence of strong shocks.

The governing equations are discretized in an unstructured triangular mesh by a cell-centered finite volume algorithm. An edge-based data structure is used to store the connectivity information and this has yielded an efficient procedure for interface flux calculations. The equations are advanced in time by an explicit, 5-stage, 2nd-order accurate, Runge-Kutta time stepping procedure. The spatial discretization considers a 2nd-oder centered scheme and two upwind schemes, namely a van Leer and a Liou flux-vector splitting scheme, with both 1st- and 2nd-order implementations. The authors believe that the form in which the Liou scheme has been implemented in the present unstructured grid context represents an original contribution, since the splitting is performed in a direction normal to the triangular cell edges. Therefore, instead of having to compute *x* and *y* splittings for a 2-D flow, only one single splitting calculation is performed per cell edge in the edge-normal direction.

The implementation of the 2nd-order versions of the two upwind schemes uses MUSCL reconstruction in order to obtain left and right states at interfaces. An original procedure for performing this reconstruction is presented which defines a 1-D stencil in the edge-normal direction and, therefore, obviates the need to compute flow property gradients at each cell. This 1-D stencil is constructed by identifying an additional triangle along the edge-normal direction which is used for the linear reconstruction process. All search operations necessary for this identification are performed at a pre-processing stage, yielding a very efficient algorithm. Moreover, the 2nd-order versions of the upwind schemes require the implementation of limiters in order to try to minimize oscillations at discontinuities. A few different limiters were actually coded, but only results with the minmod limiter were reported here. Previous experience with the other limiters has indicated that most of them fail to converge to machine zero, whereas the minmod limiter typically reaches machine zero for the cases analyzed here.

Results with unstructured fixed meshes, both coarse and fine, were obtained and compared with those calculated with an appropriate adaptively refined mesh. The various calculations indicate that it is possible to obtain converged solutions with centered schemes, even for the very high Mach number flows considered in the present work. However, these solutions will most certainly be oscillatory. Moreover, the solutions with both 1st- and 2nd-order versions of the Liou scheme are also quite oscillatory, especially across the strong upper wall entrance shock. The use of adaptively refined meshes has contributed to reduce the oscillations in all cases. On the other hand, this has not been enough to completely remove the oscillations in the cases in which they appear. The 1st-order van Leer flux vector splitting scheme has drastically reduced the flow property oscillations. However, as one could expect, this 1st-order method also causes considerable smearing of the flow discontinuities due to the excessive intrinsically added artificial dissipation.

Among the various schemes implemented, the 2nd-order AUSM$^+$ method has provided the sharpest shock definitions. This is true both with fixed and with adaptively refined meshes. However, even with the adaptively refined mesh, the 2nd-order Liou scheme has shown overshoots in the pressure distributions at the upper wall entrance shock. The situation is a lot worse for the fixed mesh solutions with this scheme. Moreover, one must also observe that both 2nd-order upwind methods have a slower convergence rate than the other schemes implemented. Furthermore, for the higher Mach number cases, the 2nd-order implementation of the Liou scheme was not able to reach machine zero, even with the minmod limiter.

The mesh adaptation procedure implemented was able to generate good quality meshes for the cases considered in the present work. The adaptation strategy identified the more relevant high gradient areas and provided an adequate grid point clustering in the important regions. Moreover, some simple mesh smoothing procedures have also been implemented, through point movement and diagonal swapping techniques, which contributed to the high quality of the meshes after refinement. It is also important to emphasize that the tests conducted in the context of the present work have only used a sensor based on flow density gradients. Although this has produced good results for the present cases, one can conceivably argue that there are other important cases in which this approach would not be the most appropriate. Therefore, further testing would clearly be necessary in order to achieve a more robust strategy for the sensor definition.

ACKNOWLEDGMENTS

The authors gratefully acknowledge the partial support for this research provided by Conselho Nacional de Desenvolvimento Científico e Tecnológico, CNPq, under the Integrated Project Research Grant Nº. 312064/2006-3. This work is also supported by Fundação de Amparo à Pesquisa do Estado de São Paulo, FAPESP, through Process Nº. 2004/16064-9.

REFERENCES

Anderson, W. K., Thomas, J. L., Van Leer, B., 1986, "A Comparison of Finite Volume Flux Vector Splittings for the Euler Equations", AIAA Journal, Vol. 24, Nº. 9, pp. 1453-1460.

Azevedo, J. L. F., 1992, "On the Development of Unstructured Grid Finite Volume Solvers for High Speed Flows", IAE, São José dos Campos, Brazil, (Report NT-075-ASE-N/92).

Azevedo, J. L. F., Figueira da Silva, L.F., 1997, "The Development of an Unstructured Grid Solver for Reactive Compressible Flow Applications", 33rd AIAA/ASME/SAE/ASEE Joint Propulsion Conference & Exhibit, Seattle, WA (AIAA Paper 97-3239).

Azevedo, J. L. F., Oliveira, L. C., 1994, "Unsteady Airfoil Flow Simulations Using the Euler Equations", Proceedings of the 12th AIAA Applied Aerodynamics Conference, Part 2, Colorado Springs, CO, pp. 650-660, (AIAA Paper 94-1892-CP).

Hirsch, C., 1990, "Numerical Computation of Internal and External Flows", Vol. 2: Computational Methods for Inviscid and Viscous Flows, Wiley, New York, Chap. 20, pp. 408-443.

Jameson, A., Mavriplis, D., 1986, "Finite Volume Solution of the Two-Dimensional Euler Equations on a Regular Triangular Mesh", AIAA Journal, Vol. 24, Nº. 4, pp. 611-618.

Jameson, A., Schmidt, W., Turkel, E., 1981, "Numerical Solution of the Euler Equations by Finite Volume Methods Using Runge-Kutta Time-Stepping Schemes", AIAA 14th Fluid and Plasma Dynamics Conference, Palo Alto, CA (AIAA Paper 81-1259).

Liou, M.S., 1994, "A Continuing Search for a Near-Perfect Numerical Flux Scheme. Part I:AUSM^{+} ", NASA Lewis Research Center, Cleveland, OH (NASA TM-106524).

Liou, M.S.,1996,"A Sequel to AUSM: AUSM^{+}", Journal of Computational Physics, Vol. 129, pp. 364-382.

Lyra, P. R. M., 1994, "Unstructured Grid Adaptive Algorithms for Fluid Dynamics and Heat Conduction", Ph.D.Thesis, Department of Civil Engineering, University of Wales Swansea, Swansea, Wales, U.K.

Mavriplis, D.J., 1988, "Multigrid Solution of the Two-Dimensional Euler Equations on Unstructured Triangular Meshes", AIAA Journal, Vol. 26, Nº.7, pp. 824-831.

Mavriplis, D.J., 1990, "Accurate Multigrid Solution of the Euler Equations on Unstructured and Adaptive Meshes", AIAA Journal, Vol. 28, Nº. 2, pp. 213-221.

Pulliam, T. H., 1986, "Artificial Dissipation Models for the Euler Equations", AIAA Journal, Vol. 24, Nº. 12, pp.1931-1940.

Steger, J. L., Warming, R. F., 1981, "Flux Vector Splitting of the Inviscid Gasdynamic Equations with Application to Finite-Difference Methods", Journal of Computational Physics, Vol. 40, Nº. 2, pp. 263-293.

Van Leer, B., 1979, "Towards the Ultimate Conservative Difference Scheme. V. A Second-Order Sequel to Godunov's Method", Journal of Computational Physics, Vol. 32, Nº. 1, pp. 101-136.

Van Leer, B., 1982, "Flux-Vector Splitting for the Euler Equations," Proceedings of the 8th International Conference on Numerical Methods in Fluid Dynamics, E. Krause, editor, Lecture Notes in Physics, Springer-Verlag, Berlin, Vol. 170, pp. 507-512.